

# Comparison of the Accuracy of Various Spatial Discretization Schemes of the Discrete Ordinates Equations in 2D Cartesian Geometry

M & C 2011

Sebastian Schunert  
Yousry Y. Azmy  
Damien Fournier  
Romain Le Tellier

May 2011

This is a preprint of a paper intended for publication in a journal or proceedings. Since changes may be made before publication, this preprint should not be cited or reproduced without permission of the author. This document was prepared as an account of work sponsored by an agency of the United States Government. Neither the United States Government nor any agency thereof, or any of their employees, makes any warranty, expressed or implied, or assumes any legal liability or responsibility for any third party's use, or the results of such use, of any information, apparatus, product or process disclosed in this report, or represents that its use by such third party would not infringe privately owned rights. The views expressed in this paper are not necessarily those of the United States Government or the sponsoring agency.

The INL is a  
U.S. Department of Energy  
National Laboratory  
operated by  
Battelle Energy Alliance



## COMPARISON OF THE ACCURACY OF VARIOUS SPATIAL DISCRETIZATION SCHEMES OF THE DISCRETE ORDINATES EQUATIONS IN 2D CARTESIAN GEOMETRY

**Sebastian Schunert and Yousry Y. Azmy**

Department of Nuclear Engineering  
North Carolina State University  
Raleigh, NC  
snschune@ncsu.edu; yyazmy@ncsu.edu

**Damien Fournier and Romain Le Tellier**

CEA, DEN, DER/SPRC/LEPh  
Cadarache, F-13108 Saint Paul-lez-Durance, France  
damien.fournier@cea.fr; romain.le-tellier@cea.fr

### ABSTRACT

We present a comprehensive error estimation of four spatial discretization schemes of the two-dimensional Discrete Ordinates ( $S_N$ ) equations on Cartesian grids utilizing a Method of Manufactured Solution (MMS) benchmark suite based on variants of Larsen's benchmark featuring different orders of smoothness of the underlying exact solution. The considered spatial discretization schemes include the arbitrarily high order transport methods of the nodal (AHOTN) and characteristic (AHOTC) types, the discontinuous Galerkin Finite Element method (DGFEM) and the recently proposed higher order diamond difference method (HODD) of spatial expansion orders 0 through 3. While AHOTN and AHOTC rely on approximate analytical solutions of the transport equation within a mesh cell, DGFEM and HODD utilize a polynomial expansion to mimic the angular flux profile across each mesh cell. Intuitively, due to the higher degree of analyticity, we expect AHOTN and AHOTC to feature superior accuracy compared with DGFEM and HODD, but at the price of potentially longer grind times and numerical instabilities. The latter disadvantages can result from the presence of exponential terms evaluated at the cell optical thickness that arise from the semi-analytical solution process. This work quantifies the order of accuracy and the magnitude of the error of all four discretization methods for different optical thicknesses, scattering ratios and degrees of smoothness of the underlying exact solutions in order to verify or contradict the aforementioned intuitive expectation.

*Key Words:* AHOT, DGFEM, HODD, Spatial Discretization, MMS.

### 1. INTRODUCTION

The mono-energetic  $S_N$  equations in Cartesian geometry comprise a linear system of hyperbolic partial differential equations that depends on the spatial variable. Over the course of the last five decades a great number of schemes have been proposed for discretizing the spatial dependence in order to obtain a fully discretized set of equations suitable for implementation on digital computers. However, no consistently best performer emerged from the set of all spatial

discretization schemes so far, even though some current preference of the community for the discontinuous Galerkin Finite Element (DGFEM) method ([1] and [2]) cannot be denied. One reason for the coexistence of a multitude of spatial discretization schemes is the large number of various requirements that spatial discretization schemes must satisfy: Accuracy, efficiency, numerical stability, robustness and resolution of the diffusion limit (cf. [3] for the last two). This paper focuses on the accuracy of four selected discretization schemes, namely the arbitrarily high order methods of the nodal (AHOTN) [4] and characteristic (AHOTC) [5] types, the discontinuous Galerkin finite element method (DGFEM) and the recently proposed higher-order diamond difference method (HODD) [6] all of orders 0 through 3. The goal of this paper is to provide a comprehensive study of the truncation error of these spatial discretization schemes on Cartesian grids, thus enabling a fair comparison of the accuracy across methods. This comparison is especially interesting because of the fundamental differences in the formalisms that led to the fully discretized set of equations of the compared methods. The arbitrarily high order methods of the nodal and characteristic type introduce a high degree of analyticity by approximately solving the transport equation within each mesh cell, while DGFEM and HODD rely on polynomial expansions within a mesh cell. The former two methods are expected to be more accurate because they take into account the physics of transport phenomena but at the cost of potentially longer grind times and instabilities originating from the evaluation of exponentials as a function of the cell optical thickness. However, recent studies published in [7] and [8] show that AHOTN and AHOTC can both be cast in an FEM framework thus furnishing a theoretical ground for comparing AHOTN and AHOTC to DGFEM and HODD based on differences in the trial space.

This paper is organized as follows. In section 2 the four discretization schemes utilized in this study are briefly introduced and differences and similarities are pointed out based on a unifying FEM framework. In Sec. 3 the test problems, which are based on an MMS benchmark suite featuring variable orders of non-smoothness of the underlying exact solution [9], are introduced. In Sec. 4 numerical results of the test problems are presented and discussed and finally, in Sec. 5, conclusions are drawn.

## 2. SPATIAL DISCRETIZATION SCHEMES

The derivation of the spatial discretization schemes starts from the  $S_N$  equations given by:

$$\begin{aligned} \mu_n \frac{\partial \psi_n}{\partial x} + \eta_n \frac{\partial \psi_n}{\partial y} + \sigma_t \psi_n(x, y) &= \sigma_s \phi(x, y) + q(x, y) \text{ if } x, y \in \mathcal{D} = (0, X) \times (0, Y) \text{ for } n \in [1, N] \\ \psi_n(x, y) &= \psi_{BC,n}(x, y) \text{ if } x, y \in \partial \mathcal{D}^- = \{x, y \in \partial \mathcal{D}, (\mu_n, \eta_n)^T \cdot \hat{n} < 0\} \\ \phi(x, y) &= \sum_{n=1}^N w_n \psi_n(x, y) \text{ with } \{(\mu_n, \eta_n), w_n\}_{n=1, \dots, N}, \end{aligned} \quad (1)$$

where the first line represents the constituting system of equations within the domain, the second line represents the boundary conditions and the third line is the quadrature rule that closes the system of equations. We denote by  $x$ ,  $y$  and  $\mu_n$ ,  $\eta_n$  the spatial variables and the direction cosines for discrete ordinate  $n$ , respectively, and by  $\sigma_t$  and  $\sigma_s$  the constant total and scattering macroscopic cross sections. The domain  $\mathcal{D}$  is rectangular with  $x \in [0, X]$  and  $y \in [0, Y]$  and is circumscribed by the boundary  $\partial \mathcal{D}$  which can be decomposed into the inflow boundary  $\partial \mathcal{D}^-$  and the outflow boundary  $\partial \mathcal{D}^+$  depending on the sign of the inner product of the directional vector

$(\mu_n, \eta_n)^T$  and the outward normal  $\hat{n}$ . Further,  $\psi_n$ ,  $\phi$  and  $q$  are the angular flux along discrete ordinate  $n$ , the scalar flux and the external body source, respectively. Finally, the angular weight of discrete ordinate  $n$  within the quadrature rule is given by  $w_n$ .

From the  $S_N$  equations we can derive a weak formulation which contains derivatives only of the test functions and a strong formulation that contains derivatives only of the trial functions [11] by multiplying Eq. 1 by a test function  $v(x, y)$  and using integration by parts once (weak formulation) or twice (strong formulation). To this end we partition the domain  $\partial\mathcal{D}$  into non-overlapping Cartesian cells  $(x_{i-1}, x_i) \times (y_{j-1}, y_j)$  with  $i = 1, \dots, I$ , and  $j = 1, \dots, J$ , covering the whole domain. The edges of the cell are divided into the exterior trace, i.e. the limit of the edge value of the flux from outside the cell, denoted by the superscript  $-$  and the interior trace, the limit of the flux edge value from inside the cell, denoted by the superscript  $+$ . For the sake of brevity we only present the final form of the strong formulation for discrete ordinates in the first angular quadrant, i.e.  $\mu_n > 0, \eta_n > 0$  (while analogous expressions apply for the other three quadrants in angular space):

$$\begin{aligned} \left( v^{(i,j)}, \left[ \mu_n \frac{\partial \psi_n^{(i,j)}}{\partial x} + \eta_n \frac{\partial \psi_n^{(i,j)}}{\partial y} + \sigma_t \psi_n^{(i,j)}(x, y) - S(x, y) \right] \right) - \mu_n \left\langle v^{(i,j)}(x_{i-1}, y), \left[ \psi_n^{(i,j)}(x_{i-1}, y) \right] \right\rangle_y \\ - \eta_n \left\langle v^{(i,j)}(x, y_{j-1}), \left[ \psi_n^{(i,j)}(x, y_{j-1}) \right] \right\rangle_x = 0, \end{aligned} \quad (2)$$

and the weak formulation:

$$\begin{aligned} \mu_n \left[ \left\langle v^{(i,j)}(x_i^+, y), \psi_n^{(i,j)}(x_i^-, y) \right\rangle_y - \left\langle v^{(i,j)}(x_{i-1}^+, y), \psi_n^{(i,j)}(x_{i-1}^-, y) \right\rangle_y \right] \\ - \eta_n \left[ \left\langle v^{(i,j)}(x, y_j^+), \psi_n^{(i,j)}(x, y_j^-) \right\rangle_x - \left\langle v^{(i,j)}(x, y_{j-1}^+), \psi_n^{(i,j)}(x, y_{j-1}^-) \right\rangle_x \right] \\ - \mu_n \left( \frac{\partial v^{(i,j)}}{\partial x}, \psi_n^{(i,j)}(x, y) \right) - \eta_n \left( \frac{\partial v^{(i,j)}}{\partial y}, \psi_n^{(i,j)}(x, y) \right) + \left( v^{(i,j)}, \sigma_t \psi_n^{(i,j)}(x, y) - S(x, y) \right) = 0. \end{aligned} \quad (3)$$

where the jump operator is defined as  $[[g]] = g(\mathbf{r}^+) - g(\mathbf{r}^-)$ ,  $\mathbf{r}$  is the spatial vector and  $S(x, y) = \sigma_s \phi + q(x, y)$ . Moreover in Eqs. 2 and 3 the following definitions are used:

$$\begin{aligned} \langle g(x), f(x) \rangle_x &= \int_{x_{i-1}}^{x_i} dx g(x) f(x) \\ (g(x, y), f(x, y)) &= \int_{x_{i-1}}^{x_i} \int_{y_{j-1}}^{y_j} dx dy g(x, y) f(x, y). \end{aligned} \quad (4)$$

While on the inflow edges the exterior trace is naturally given by the appropriate angular flux from the upstream cell, we need to prescribe how to calculate the flux on the exterior trace on outflow edges. To this end we set the exterior trace equal to the interior trace on all outgoing edges which in general is referred to as upstreaming. In analogy to Eqs. 2 and 3 this condition is enforced only in an integral sense such that e.g. for the right edge we obtain:

$$\left\langle v^{(i,j)}(x_i^+, y), \psi(x_i^-, y) - \psi(x_i^+, y) \right\rangle_y = 0, \quad (5)$$

where  $\psi(x_i^-, y)$  is the flux expansion on the exterior trace and  $\psi(x_i^+, y) = \psi(x_i, y)$  is the limit of the flux value from inside the cell. Together with the analogous expression on the top outgoing

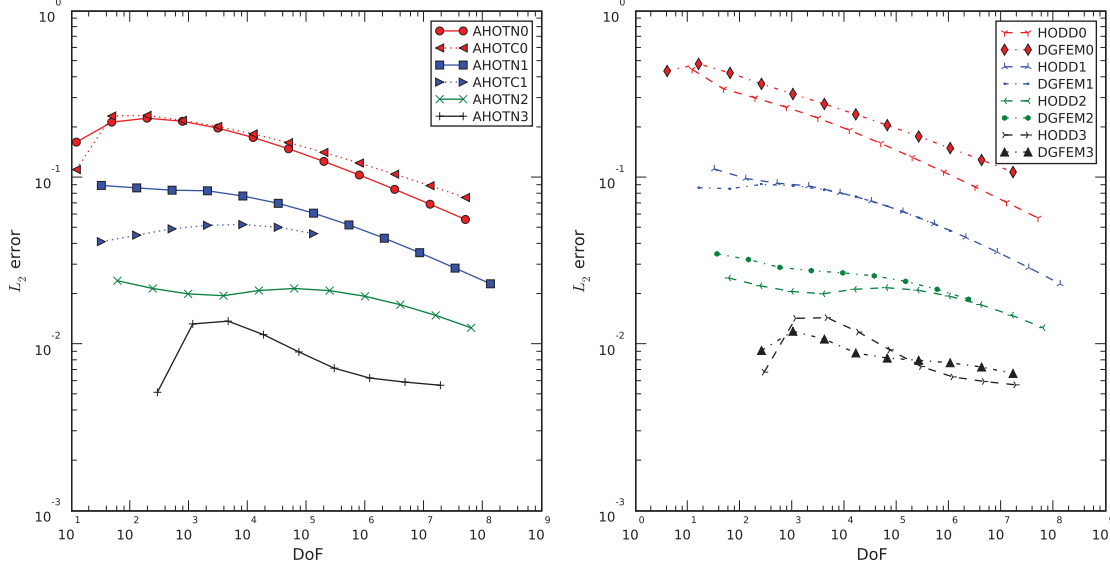


Figure 1:  $L_2$  error vs. degrees of freedom (DoF) for test case I0.

edge we refer to Eq. 5 as the integral upstream relation. In the presented work we use the strong form to derive AHOTN, HODD and AHOTC while DGFEM is traditionally derived via the weak form. However, all employed trial and test spaces are sufficiently smooth implying equivalence of the weak and strong form. Hence, the choice which one to use for the derivation of a discretization scheme is a matter of convenience, not necessity.

For the sake of simplicity the cell indices  $i, j$  and the discrete ordinate index  $n$  are dropped whenever the context allows. Throughout the remainder of the paper let  $(x_m, y_m)$  denote the coordinates of the cell midpoint of an arbitrary mesh cell with dimensions  $(\Delta x, \Delta y)$  and define the scaled variables  $\tilde{x} = 2(x - x_m)/\Delta x$  and  $\tilde{y} = 2(y - y_m)/\Delta y$ .

## 2.1 DGFEM

For DGFEM of order  $\Lambda$  the trial functions as well as the test functions are selected from the set of Legendre Polynomials of orders 0 to  $\Lambda$ :

$$\psi(x, y) = \sum_{l=0}^{\Lambda} \sum_{k=0}^{\Lambda} (2l+1)(2k+1) \bar{\psi}_{l,k} P_l(\tilde{x}) P_k(\tilde{y})$$

$$v_{r,s}(x, y) = P_r(\tilde{x}) P_s(\tilde{y}) \text{ with } r, s = 0, \dots, \Lambda, \quad (6)$$

where  $\bar{\psi}_{l,k}$  are Legendre moments of  $\psi(x, y)$  given by:

$$\bar{\psi}_{l,k} = \frac{1}{\Delta x \Delta y} (P_l(\tilde{x}) P_k(\tilde{y}), \psi(x, y)). \quad (7)$$

Additionally, the flux on the exterior trace is similarly expanded into Legendre Polynomials, e.g. for the left edge:

$$\psi(x_{i-1}^-, y) = \sum_{k=0}^{\Lambda} (2k+1) \bar{\psi}_k(x_{i-1}^-) P_k(\tilde{y}), \quad (8)$$

with the edge flux moments being defined by:

$$\bar{\psi}_k(x_{i-1}^-) = \frac{1}{\Delta y} \left\langle P_k(\tilde{y}), \psi(x_{i-1}^-, y) \right\rangle_y. \quad (9)$$

The DGFEM system of equations can be obtained by substituting the trial and test space Eq. 6 and the expansion on the exterior traces Eq. 8 into the weak formulation Eq. 3 and the integral upstream relation Eq. 5. For DGFEM the number of degrees of freedom per mesh cell and angle is then given by  $\text{DoF}_{pc}^{DGFEM} = (\Lambda + 1)^2$ . It is important to point out here that in contrast to the other three spatial discretization schemes, the outgoing edge flux moments are not additional variables since they are linearly dependent on the cell Legendre moments.

## 2.2 AHOTN

As first presented in [7] the AHOTN equations can be obtained using the following trial and test spaces:

$$\begin{aligned} \psi(x, y) &= \sum_{l=-1}^{\Lambda} \sum_{k=0}^{\Lambda} a_{lk} \xi_l(x) P_k(\tilde{y}) + \sum_{k=-1}^{\Lambda} \sum_{l=0}^{\Lambda} b_{lk} \xi_k(y) P_l(\tilde{x}) + \sum_{l=0}^{\Lambda} \sum_{k=0}^{\Lambda} c_{lk} P_l(\tilde{x}) P_k(\tilde{y}) \\ v_{r,s} &= P_r(\tilde{x}) P_s(\tilde{y}) \text{ with } r, s = 0, \dots, \Lambda, \end{aligned} \quad (10)$$

with the additional restriction on the expansion coefficients that:

$$\begin{aligned} \left( v_{r,s}, \left[ \sum_{l=-1}^{\Lambda} \sum_{k=0}^{\Lambda} a_{lk} \xi_l(x) P_k(\tilde{y}) \right] \right) &= \frac{c_{rs}}{(2r+1)(2s+1)} \\ \left( v_{r,s}, \left[ \sum_{k=-1}^{\Lambda} \sum_{l=0}^{\Lambda} b_{lk} \xi_k(y) P_l(\tilde{x}) \right] \right) &= \frac{c_{rs}}{(2r+1)(2s+1)} \quad r, s = 0, \dots, \Lambda, \end{aligned} \quad (11)$$

where the function  $\xi_l(x)$  is defined as:

$$\begin{aligned} \xi_{-1}(x) &= \exp\left(-\frac{\sigma_t \Delta x}{2\mu} (\tilde{x} + 1)\right) \\ \xi_k(x) &= \frac{\sigma_t \Delta x}{2\mu} \int_{-1}^{\tilde{x}} du \exp\left(-\frac{\sigma_t \Delta x}{2\mu} (\tilde{x} - u)\right) P(u). \end{aligned} \quad (12)$$

Note that for obtaining the corresponding relation to Eq. 12 in  $y$ ,  $\mu$  is replaced by  $\eta$ , and for discrete ordinates in the second through fourth angular quadrant  $\xi_k(x)$  must be slightly modified[7]. For AHOTN the total number of degrees of freedom per cell is  $\text{DoF}_{pc}^{AHOTN} = (\Lambda + 1)^2 + 2(\Lambda + 1)$ .

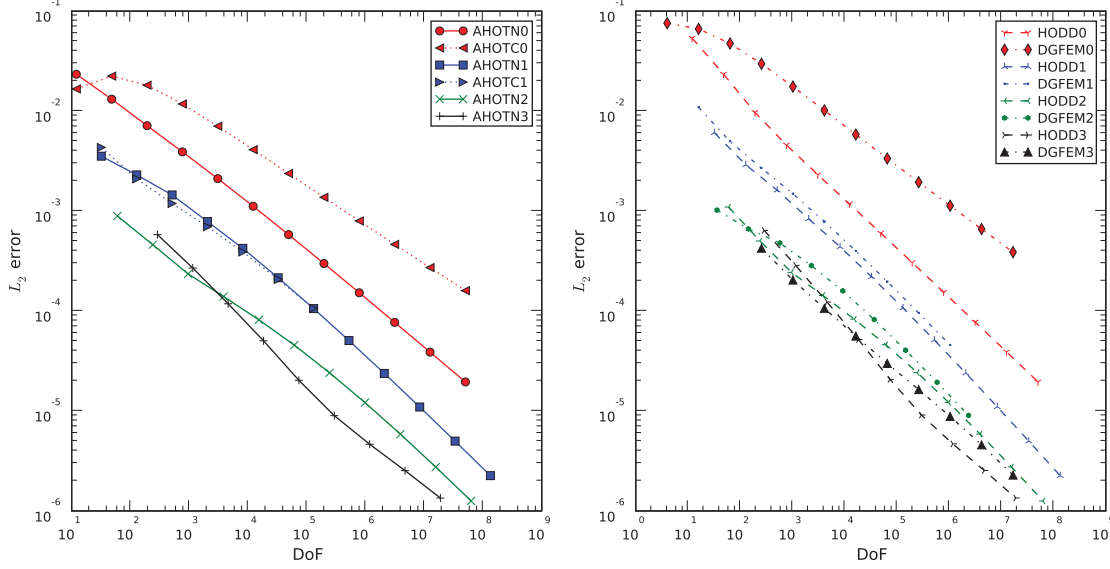


Figure 2:  $L_2$  error vs. degrees of freedom (DoF) for test case I1.

### 2.3 HODD

For the derivation of the HODD method

$$\begin{aligned}
 \psi(x, y) = & \sum_{l=0}^{\Lambda} \sum_{k=0}^{\Lambda} (2l+1)(2k+1) \bar{\psi}_{l,k} P_l(\tilde{x}) P_k(\tilde{y}) + \sum_{k=0}^{\Lambda} (2\Lambda+3)(2k+1) a_k P_k(\tilde{y}) P_{\Lambda+1}(\tilde{x}) \\
 & + \sum_{l=0}^{\Lambda} (2\Lambda+3)(2l+1) b_l P_l(\tilde{x}) P_{\Lambda+1}(\tilde{y}) \\
 v_{r,s} = & P_r(\tilde{x}) P_s(\tilde{y}) \text{ with } r, s = 0, \dots, \Lambda,
 \end{aligned} \tag{13}$$

are used as trial and test space, respectively. Further, on the exterior traces of each edge we assume the flux to be expanded as in Eq. 8. In order to derive the constituting system of equations we first constrain the function space to accomodate weakly imposed essential boundary conditions on the inflow boundary of each cell:

$$\begin{aligned}
 \left\langle v^{(i,j)}(x_{i-1}, y), \left[ \left[ \psi_n^{(i,j)}(x_{i-1}, y) \right] \right]_y \right\rangle &= 0 \\
 \left\langle v^{(i,j)}(x, y_{j-1}), \left[ \left[ \psi_n^{(i,j)}(x, y_{j-1}) \right] \right]_x \right\rangle &= 0,
 \end{aligned} \tag{14}$$

such that the respective term in the strong formulation Eq. 2 can be dropped. Then we substitute the trial and test space Eq. 13 and the expansion on the exterior edges Eq. 8 into the remainder of the strong form and the integral upstream relation Eq. 5. Subsequently, the conditions originating from the integral upstream relations are used to eliminate  $a_k$  and  $b_l$  from the remaining equations. The emerging system of equations can finally be cast into the form given in [6]. The number of degrees of freedom per cell and angle for HODD is given by  $\text{DoF}_{pc}^{\text{HODD}} = (\Lambda+1)^2 + 2(\Lambda+1)$ . We point out that the HODD method of order zero is the standard Diamond Difference scheme.

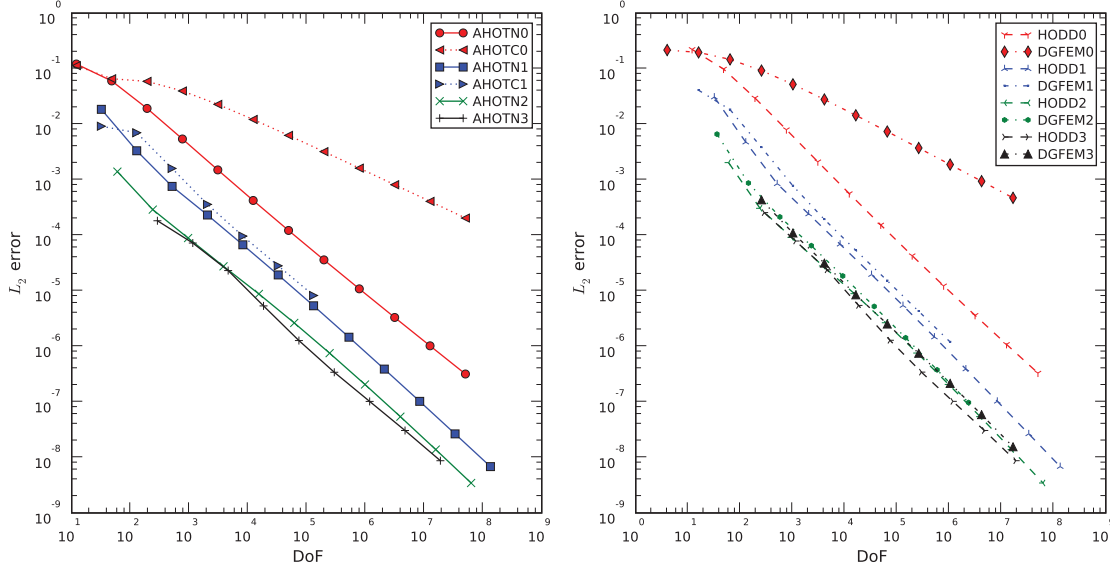


Figure 3:  $L_2$  error vs. degrees of freedom (DoF) for test case I2.

## 2.4 AHOTC

The reformulation of the AHOTC method as an FEM method is reported in [8]. Akin to the reformulation of the transport equation in its characteristic form, the test and trial spaces are formulated in terms of the distance along the characteristic  $t$  such that in an arbitrary spatial mesh cell  $\mathbf{r} = \mathbf{r}_0 + t(\mu, \eta)^T$  where  $\mathbf{r}_0 = (x_0, y_0)^T$  is a point on the inflow boundary. Note that the mapping  $x, y \rightarrow \mathbf{r}, t$  is surjective and hence it can be inverted such that we can associate a pair  $x, y$  with a unique  $\mathbf{r}_0, t$ . As a consequence, even if the trial and test space are formulated in terms of  $\mathbf{r}_0$  and  $t$  an integration over  $x, y$  can be carried out by performing an appropriate change of variables. Further, for the sake of consistency with [8], monomials are used instead of Legendre Polynomials for the definition of the trial and test spaces:

$$\psi(\mathbf{r}_0 + t(\mu, \eta)^T) = \sum_{k=0}^{\Lambda} a_k z_0^k \exp(-\sigma_t t) + \sum_{l=0}^{\Lambda} \sum_{k=0}^{\Lambda} b_{lk} \int_0^t ds (x_0 + t\mu)^l (y_0 + t\eta)^k \exp(-\sigma_t(t-s)),$$

$$v_{r,s} = x^r y^s \text{ with } r, s = 0, \dots, \Lambda. \quad (15)$$

where  $z_0$  is either  $x_0$  on the bottom inflow edge or  $y_0$  on the left inflow edge. The number of degrees of freedom per cell and angle for AHOTC is given by  $\text{DoF}_{pc}^{AHOTC} = (\Lambda + 1)^2 + 2(\Lambda + 1)$ .

## 3. BENCHMARK TEST CASES

In this work we use the Method of Manufactured Solutions (MMS) benchmark suite MSBS-2D outlined in [9] to create the test cases that the comprehensive error estimation is based on. MSBS-2D creates a manufactured solution to the transport problem Eq. 1 comprised of



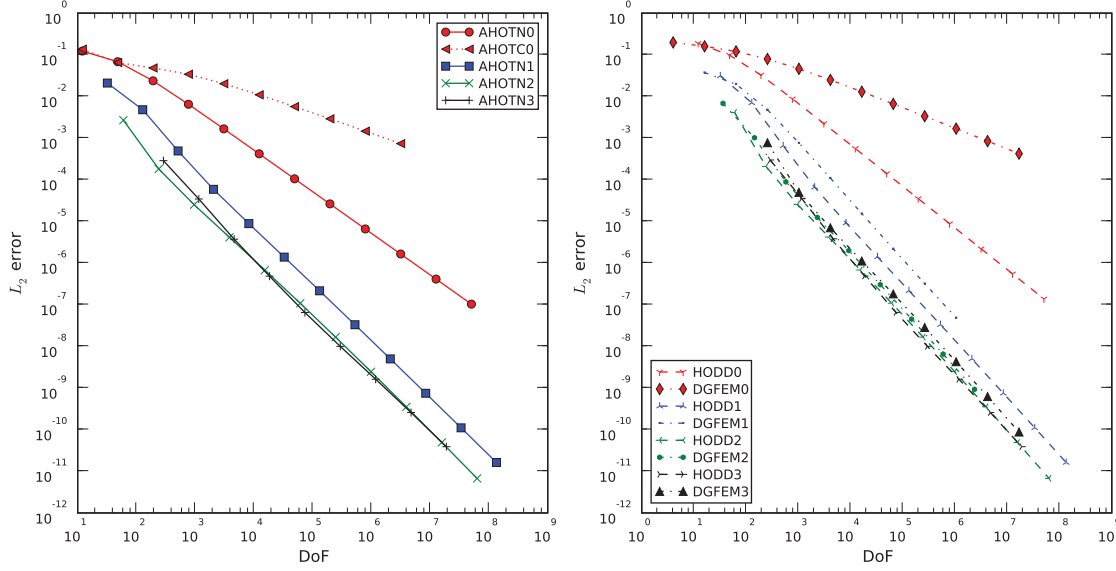


Figure 4:  $L_2$  error vs. degrees of freedom (DoF) for test case I3.

cell Legendre moments up to arbitrary order of the source  $q(x, y)$  and the exact angular flux solution  $\psi(x, y)$  upon providing the input parameters: The total and scattering cross sections  $\sigma_t$  and  $\sigma_s$ , a quadrature rule  $\{(\mu_n, \eta_n), w_n\}_{n=1, \dots, N}$ , a Cartesian mesh, the domain size  $X$  and  $Y$ , boundary conditions and the parameter  $Q$ . The benchmark suite features a variable degree of smoothness of the exact solution denoted by  $Cp$  where  $p$  is the highest order up to which all partial derivatives are bounded. The smoothness can be controlled via the boundary conditions and the parameter  $Q$ . For all presented test cases the  $S_4$  fully symmetric quadrature and a square domain with  $X = Y = 1$  are employed, and the domain is subdivided into  $2^I \times 2^I$  uniform mesh cells with  $I = 1, \dots, 12$ ; choices for the remaining parameters for all test cases are presented in Table I, where  $\psi_{<B/T>,n}$  and  $\psi_{<L/R>,n}$  are boundary conditions on the domain's bottom/top and left/right boundary, respectively, with

$$\begin{aligned}\bar{x} &= \frac{1 - \text{sign}(\mu_n)}{2}X + \text{sign}(\mu_n)x \\ \bar{y} &= \frac{1 - \text{sign}(\eta_n)}{2}Y + \text{sign}(\eta_n)y.\end{aligned}\tag{16}$$

For the sake of consistency with the physical meaning of the source, all reference solutions feature strictly positive sources. We denote the spatial expansion order of a spatial discretization scheme by appending its acronym with the corresponding integer, e.g. AHOTN1 is AHOTN of order 1. For the most part, the spatial discretization error is measured in a discrete  $L_2$  norm given by:

$$\|\epsilon\|_2 = \left( \sum_{n=1}^N w_n \sum_{i=1}^{2^I} \sum_{j=1}^{2^I} \Delta x_i \Delta y_j \left( \bar{\psi}_{n,0,0}^{(i,j)} - \bar{\psi}_{n,0,0}^{(i,j),ref} \right)^2 \right)^{\frac{1}{2}}, \tag{17}$$

which in the remainder of this paper is simply referred to as  $L_2$  error. Note that the exact (MMS) cell average is compared to the computed cell average on the same mesh that the

**Table I: Parameter set for the test cases used in the error estimation.**

Test Case	$Cp$	$\sigma_t$	$c = \frac{\sigma_s}{\sigma_t}$	$Q$	$\psi_{<L/R>,n}$	$\psi_{<B/T>,n}$
I0	0	1.0	0.2	1.0	5	0
I1	1	1.0	0.2	1.0	0	0
I2	2	1.0	0.2	1.0	$1 + 4\bar{y}^2$	$1 + 4\bar{x}^2$
I3	3	1.0	0.2	1.0	$1 + 4\bar{y}^3$	$1 + 4\bar{x}^3$
II0	0	10.0	0.2	10.0	5	0
II1	1	10.0	0.2	10.0	0	0
III1	1	1.0	0.8	1.0	0	0
IV1	1	10.0	0.8	10.0	0	0

numerical solution is obtained on. Alternatively we can apply the error norm Eq. 17 by first reconstructing the numerical flux solution and then prolonging it onto the finest mesh  $I_F = 12(9)$ ; the error norm Eq. 17 is then applied on the finest mesh refinement level. We will refer to this error as prolonged  $L_2$  error. Throughout the discussion of the numerical results we refer to the number of degrees of freedom DoF as the product of the number of mesh cells and the number of degrees of freedom per cell  $\text{DoF} = 2^{2I} \cdot \text{DoF}_{pc}$ ; further the asymptotic rate of convergence roc is the slope (on a log-log scale) of the error vs. DoF curve computed from the last two levels of mesh refinement:

$$\text{roc} = \log_2 \left( \frac{\|\epsilon\|_{2,I_F}}{\|\epsilon\|_{2,I_{F-1}}} \right). \quad (18)$$

The computation of the AHOTN, AHOTC and HODD results was performed using a test code at NCSU, while the DGFEM results with exception of the zeroth order<sup>1</sup> stem from calculations with the SNATCH solver [1] of the ERANOS code system [12]. As the SNATCH solver is meant to work on locally refined non-conforming grids it consequently suffers from memory footprint overhead on uniform grids which restricts it to meshes with at most  $2^9 \times 2^9$  cells ( $I_F = 9$ ). In contrast the NCSU solver did not suffer from this restriction.

#### 4. NUMERICAL RESULTS

Numerical results of the error estimation study are presented in Figs. 1 to 8 and Table II. In Figs. 1 to 4 optically thin cases ( $\sigma_t = 1.0$ ) with varying smoothness C0 through C3, respectively, are plotted. In real transport problems the smoothness is in general limited either to C0 in certain shielding configurations with shadowing, e.g. only a segment of the domain is illuminated, or to C1 for configurations featuring vacuum boundary conditions (e.g. reactor physics problems). The two test cases I0 and I1 presented in Figs. 1 and 2 simplistically capture the essentials of a shadowing and reactor physics problem, respectively. The test cases I2 and I3 are unrealistic in the sense that no real problem features smoothness levels higher than C1. Following the results for the optically thin test cases, Figs. 5 and 6 show optically thick test cases with  $\sigma_t = 10.0$  for smoothness C0 and C1. To enable an easier comparison across methods, Fig. 7 plots results of all linear schemes together for both  $\sigma_t = 1.0$  and  $\sigma_t = 10.0$  and a C1 test case. Subsequently,

<sup>1</sup>The zeroth order DGFEM scheme, although usually not referred to as such is the well-known Step Method.

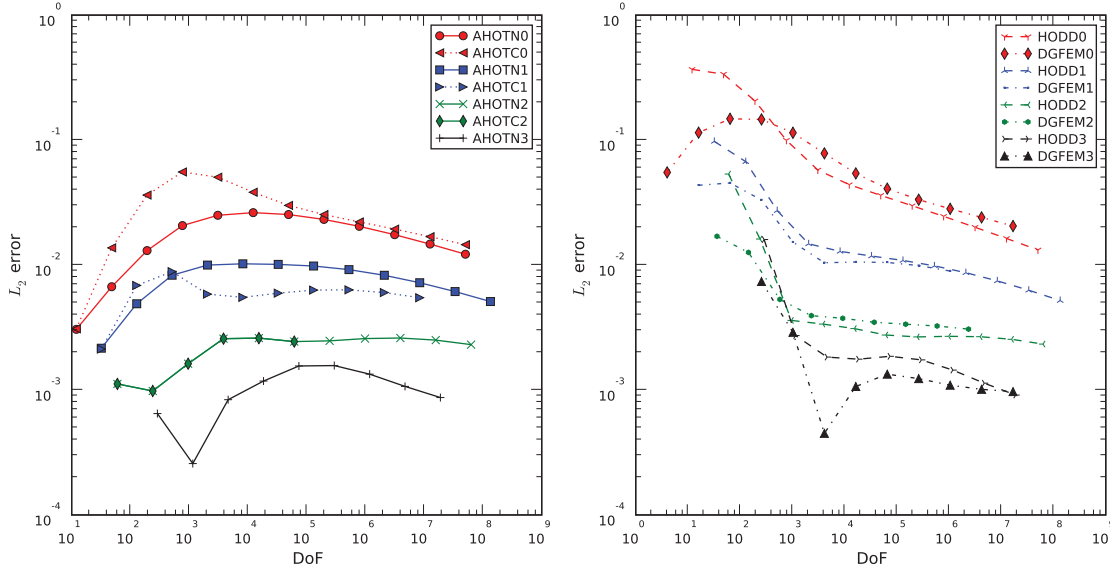


Figure 5:  $L_2$  error vs. degrees of freedom (DoF) for test case II0.

Fig. 8 illustrates how employing the flux prolongation for computing the discrete error norm Eq. 17 affects the shape of the error vs. DoF curves in the presence of (a) non-smoothness (in conjunction with high spatial expansion orders) and (b) boundary layers. Finally, in Table II asymptotic rates of convergence for all considered test cases are summarized.

#### 4.1 General Discussion

It should first be noted that even for limited levels of smoothness (C0 and C1) increasing the order of the spatial expansion does improve the accuracy of the numerical results across all methods, albeit not the asymptotic rate of convergence (see Figs. 1, 2, 5 and 6). When the smoothness is increased to C2 and finally to C3, depicted in Figs 3 and 4, respectively, higher spatial order methods also start benefiting from the larger rate of convergence permitted by the increased smoothness in addition to their superior accuracy even in the case of limited smoothness. The difference is most pronounced for a first order accurate method like AHOTC0 (Step Characteristic) compared to e.g. AHOTN3 for test case I3 plotted in Fig. 4. For the last mesh refinement level the difference in accuracy is about five orders of magnitude. However, recalling that in practical applications the smoothness is limited to C1 we conclude that the differences in accuracy between lower and higher order schemes are not quite as drastic in reality: In Fig. 2 (I1 test case) the same comparison between AHOTC0 and AHOTN3 gives a difference of about two to three orders of magnitude.

For several cases throughout the error estimation study maxima occur in the error vs. DoF curves resulting in computed errors that are smaller on coarse meshes than on finer meshes. One mechanism that explains the occurrence of maxima, the boundary layer effect, is discussed in the next subsection. However, for the C0 test case and high spatial expansion orders ( $\Lambda = 2, 3$ ) respective error vs. DoF curves exhibit further peculiar features such as minima ( $\sigma_t = 10.0$  only) and change of curvature throughout the mesh refinement study. These features cannot

be solely attributed to the boundary layer effect, but are related to the employed discrete error norm in conjunction with limited smoothness as these features only appear for C0 test cases. The conclusion that the described features are caused also by the error norm is substantiated by computing the error on the finest mesh via prolongation of the flux reconstruction of the numerical solution. In Fig. 8 (a) we see that for both AHOTN3 and HODD3 a smoother error vs. DoF curve is obtained for the I0 test case if the error is computed on the finest mesh. It should be stressed here that errors computed from a prolongation do not show the expected asymptotic behavior (constant rate of convergence) for meshes too close to the reference mesh, because the prolongation operator depends on the mesh that the numerical solution is obtained on and the mesh that it is prolonged to. For meshes far from the finest mesh, the change of the prolongation operator from one to another refinement level is small, but very close to the finest mesh the change of the prolongation operator from one mesh refinement level to the next is noticeable and is reflected in the increasing slope. However, the prolongation procedure potentially yields the asymptotic slope on coarse meshes without suffering from pre-asymptotic behavior.

## 4.2 Boundary Layer Effect

The occurrence of maxima in some DoF versus error plots (e.g. Fig. 5) can at least partially be attributed to boundary layer effects. For sufficiently large  $\sigma_t$  the manufactured solution that is employed in the framework of this paper (cf. [9]) exhibits steep gradients close to the boundary of the domain and a very slowly varying solution within the domain. On coarse meshes the steep gradient gets smeared over the extent of a comparably much larger mesh cell such that only a very small fraction of the cell is actually occupied by the boundary layer while most of the cell features a very slowly varying underlying exact solution. Since we use the discretized error norm Eq. 17 solely based on the difference of the averages of the exact and numerical solution we do allow cancellation of errors across the mesh cell. The numerical solution on the coarse grid is accurate for the very slowly varying function within the domain but completely inadequate for the boundary layer, but due to the small fraction of the area of the mesh cells that the boundary layer occupies the error committed in the boundary layer does not alter the cell average much. Hence, the computed  $L_2$  error is very small. The occurrence of a maximum in the error versus DoF curve can be attributed to the growing fraction of the edge cell's area occupied by the boundary layer as the mesh is refined. The maximum occurs when the mesh cell's width is approximately equal to the width of the boundary layer such that no smearing of the steep gradient across a comparably large cell can occur but the level of mesh refinement is still inadequate for resolving the boundary layer. After the occurrence of the maximum further refinement of the mesh starts to adequately resolve the boundary layer such that the total error decreases. Note that the occurrence of maxima is a consequence of using the discrete error norm Eq. 17 without prolongation. In Fig. 8 (b) we plot the  $L_2$  error vs. degrees of freedom for the II0 test case and AHOTN with spatial expansion orders zero and one first without and then with prolongation. The  $L_2$  error for the case with prolongation does not exhibit maxima, because the prolongation procedure forces the coarse mesh solution to resolve the structure of the boundary layer and thus eliminates smearing across the coarse mesh cell.

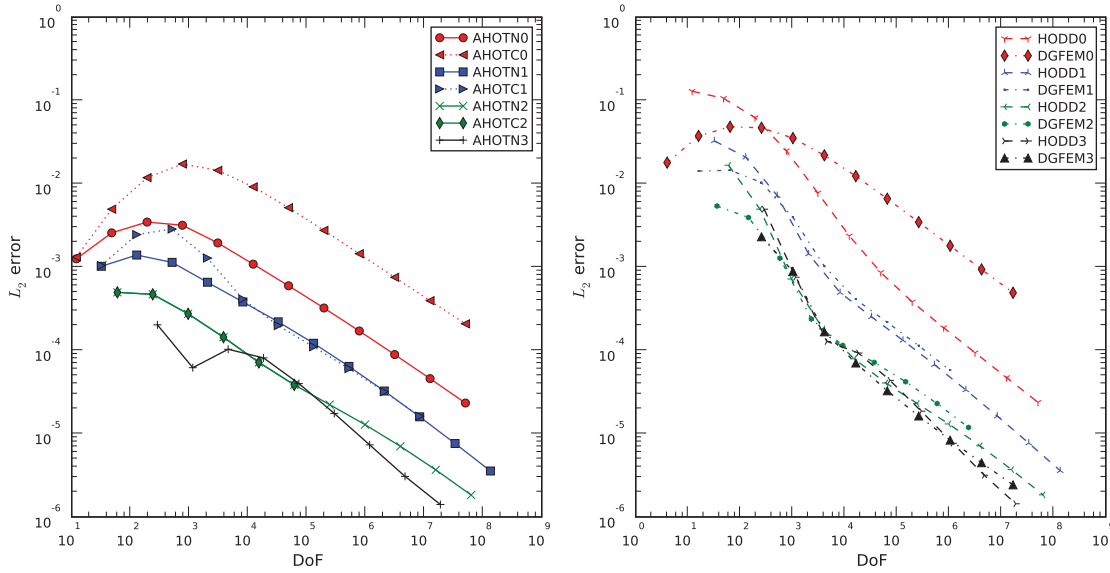
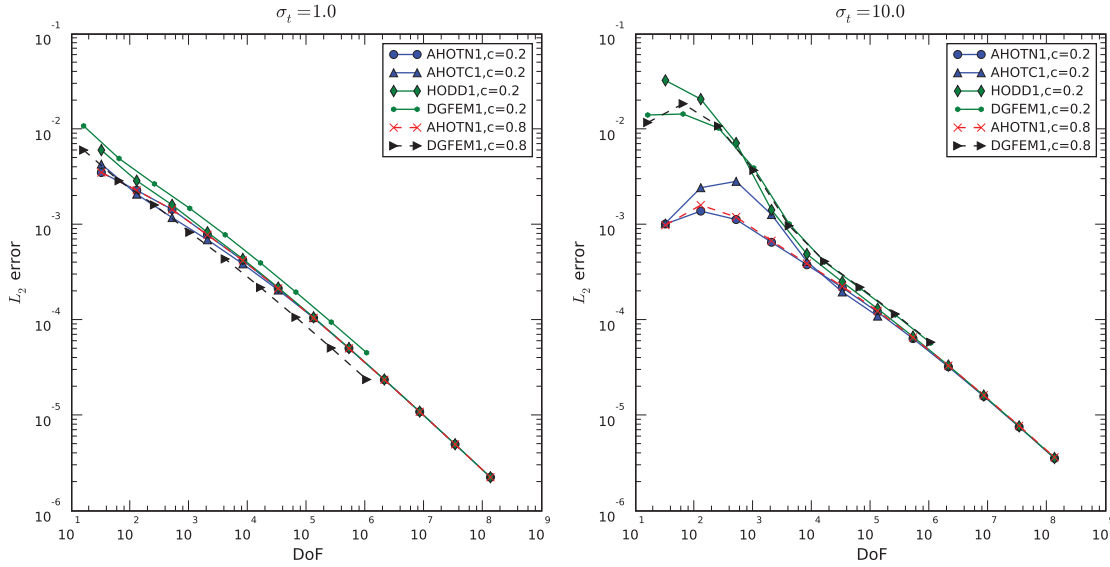


Figure 6:  $L_2$  error vs. degrees of freedom (DoF) for test case III.1.

### 4.3 Comparison across Spatial Discretization Schemes

The discussion of the accuracy across discretization schemes is divided into the discussion of the optically thin problems Figs. 1 to 4 and the optically thick problems Figs. 5 and 6. In general AHOTC results are only available up to  $\Lambda = 1$  as the employed AHOTC implementation becomes numerically unstable for  $\Lambda > 1$  for almost all mesh refinement levels and for  $\Lambda = 1$  if the mesh cells are sufficiently optically thin (last 4-5 refinement levels). The described numerical instabilities are a direct consequence of the presence of exponential functions in the AHOTC system of equations. In principle, similar instabilities occur for AHOTN, but they first tend to occur only for  $\Lambda > 1$  and optically thinner cells and second in the optically thin cell limit asymptotic expansions of the spatial weights are used to circumvent the problem of the instabilities [13]. A comprehensive study and solution of the AHOTC instability problem is proposed in [8]. For optically thin problems, the difference between the accuracy of the four methods is in general negligible for any degree of smoothness and all mesh refinement levels with the exception of the zeroth spatial order methods. In the C0 case, AHOTC0 (Step Characteristic) and AHOTN0 perform very similar for optically thick cells, but for optically thin cells AHOTN0 is superior since it features a higher asymptotic rate of convergence. The least accurate zeroth order scheme is DGFEM0 (Step Method) throughout all mesh refinement levels. Finally, HODD0 (Diamond Difference) is equivalent to AHOTN in the fine mesh limit and only performs slightly worse for coarser meshes. Moving on to the smoother test cases C1 to C3, the only difference is that the performance of AHOTC0 deteriorates in comparison with AHOTN0 and HODD0 which is caused by the larger rate of convergence of AHOTN0 and HODD0 facilitated by the increased level of smoothness of the C1 to C3 test cases. In summary, for problem configurations featuring an optically thin domain virtually no advantage is gained when using AHOTN or AHOTC versus DGFEM or HODD.

In the case of optically thick domains with  $\sigma_t = 10.0$  depicted in Figs. 5 and 6 some ad-



**Figure 7:**  $L_2$  error vs. degrees of freedom (DoF) for test cases I1 and III1 (left) and III1 and IV1 (right).

vantage can be gained from using AHOTN or AHOTC vs. HODD and DGFEM on relatively coarse meshes. However, for the C0 test problem depicted in Fig. 5 the comparison of AHOTN/AHOTC versus DGFEM/HODD suffers from the occurrence of maxima in the AHOTN and AHOTC curves. The validity of error values obtained on a grid that is coarser than the grid which the maximum error is obtained for might be questionable. However, we point out that the high accuracy of coarse mesh solutions is caused by cancellation of error and that the actual cell average values are indeed close to the reference cell average values. Hence, a comparison of the results for the C0 test configuration is valid even for very coarse meshes. The difference in accuracy between AHOTN/AHOTC and DGFEM/HODD for the C0 test case can be as much as 1-2 orders of magnitude on the coarsest meshes. In contrast the C1 configuration does not develop maxima as pronounced as the C0 test case. As a consequence AHOTN and AHOTC are not only more accurate for meshes on the left of the maximum (1-2 orders of magnitude), but also for meshes to the right of the maximum. As an example, the error obtained with AHOTN1 on mesh refinement level three is six times smaller than the error obtained with HODD1 or DGFEM1 for the same number of degrees of freedom. Qualitatively, the same is true for the obtained AHOTC results, but for AHOTC1 the error is slightly larger than the AHOTN1 error, but still smaller than the HODD and DGFEM errors. As the mesh is refined the difference vanishes and only marginal differences between the four discretization schemes remain. The difference among the four discretization schemes for a C1 test case and linear spatial order can also be inferred from Fig. 7. For optically thin test cases (left side) virtually no difference exists between the four methods while for optically thick test cases (right) noticeable differences are visible for coarse meshes. Finally, Fig. 7 also includes results of cases III and IV thus testing the influence of the scattering ratio on the  $L_2$  error norm which is found to be negligible. In conclusion, we assert that AHOTN and AHOTC feature a superior accuracy on coarse meshes for both C0 and C1 test problems for optically thick domains.

**Table II: Asymptotic rates of convergence for various spatial expansion orders, discretization schemes, levels of smoothness and material properties. For test cases I-IV rates of convergence are ordered like I/II/III/IV. For some cases data is not available (n.a.).**

Discr. Scheme	Cp	$\Lambda = 0$	$\Lambda = 1$	$\Lambda = 2$	$\Lambda = 3$
AHOTN	C0	0.3/0.27	0.31/0.26	0.25/0.12	0.06/0.3
	C1	0.99/0.97	1.15/1.1/1.15/1.1	1.13/1.0	0.91/1.12
	C2	1.69	1.96	2.0	1.81
	C3	2.0	2.77	2.87	2.73
AHOTC	C0	0.24/0.21	0.18/0.19	n.a.	n.a.
	C1	0.77/0.92	1.0/1.01	n.a.	n.a.
	C2	1.0	1.8	n.a.	n.a.
	C3	1.0	n.a.	n.a.	n.a.
HODD	C0	0.31/0.3	0.32/0.27	0.25/0.13	0.07/0.32
	C1	1.0/0.99	1.15/1.1	1.13/1.01	0.91/1.13
	C2	1.72	1.96	2.0	1.81
	C3	2.0	2.77	2.87	2.73
DGFEM	C0	0.24/0.23	0.26/0.15	0.26/0.08	0.13/0.02
	C1	0.77/0.93	1.05/0.98/1.07/0.98	1.1/0.95	1.01/0.88
	C2	1.0	1.83	1.95	1.87
	C3	1.0	2.73	2.78	2.73

Finally, in Table II we present the asymptotic rates of convergence for all considered test cases. The table illustrates that the rate of convergence is limited by either the spatial expansion order or the smoothness of the exact solution, whichever is smaller. The obtained rates of convergence vary strongly across different levels of smoothness, spatial expansion orders and weakly among the employed discretization schemes but are not sensitive to the material properties. It should be stressed that asymptotic rates of convergence are only meaningful if the scheme exhibits asymptotic behavior within the last two mesh refinement levels. This is not the case for all presented results, in particular not for the C0 test cases.

## 5. CONCLUSIONS

We presented a comprehensive error analysis of four spatial discretization schemes: AHOTN, AHOTC, DGFEM and HODD. The differences and similarities among the four methods were reduced to the differences in the trial spaces within a FEM framework. Based on MMS benchmark configurations created with the code MSBS-2D we tested the accuracy of the four contestants via numerical experiments. The outcome confirms the aforementioned intuition that the high degree of analyticity present in AHOTN and AHOTC allows superior accuracy on coarse meshes but results on reasonably fine meshes differ only marginally.



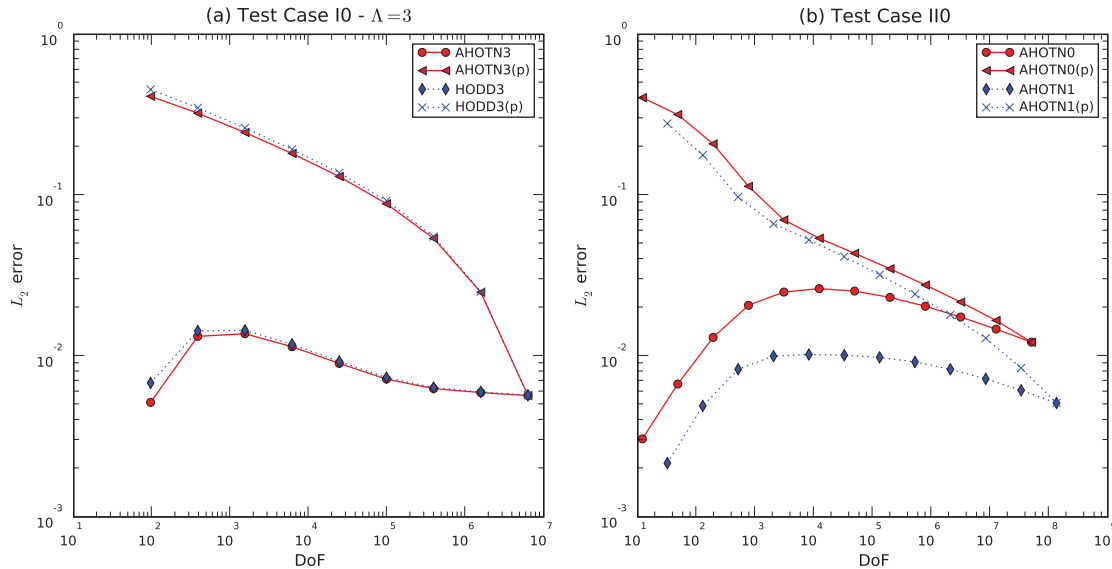


Figure 8: (a)  $L_2$  error obtained by prolongation (p) and standard  $L_2$  error for AHOTN3 and HODD3 for the I0 test case. (b)  $L_2$  error for test case II0 obtained with (p) and without prolongation to the finest mesh for AHOTN0 and AHOTN1.

## REFERENCES

1. L. Gastaldo, R. Le Tellier, C. Suteau, D. Fournier, and J. M. Ruggieri. High-order Discrete Ordinate Transport in Non-Conforming 2D Cartesian Meshes. In *International Conference on Mathematics, Computational Methods & Reactor Physics, M&C 2009, Saratoga Springs, New York*, 2009.
2. Reed, W.H. and Hill, T.R. Triangular Mesh Methods for the Neutron Transport Equation, LA-UR-73-479 (1973).
3. Adams, M.L. Discontinuous Finite Element Transport Solutions in Thick Diffusive Problems. *Nucl. Sci. Eng.*, **137**, pp. 298-333 (2002).
4. Azmy Y.Y. The Weighted Diamond Difference Form of Nodal Transport Methods. *Nucl. Sci. Eng.*, **98**, pp. 29-40 (1988).
5. Azmy Y.Y. Arbitrarily High Order Characteristic Methods for Solving the Neutron Transport Equations. *Annals of Nuclear Energy*, **19**, pp. 593-606 (1992).
6. Hebert, A. High Order Diamond Differencing Schemes. *Annals of Nuclear Energy*, **33**, pp. 1479-1488 (2006).
7. Duo, J.I. and Azmy, Y.Y. and Zikatanov, L.T. A-posteriori Error Estimator and AMR for Discrete Ordinates Nodal Transport Methods. *Annals of Nuclear Energy*, **36**, pp. 268-273 (2006).
8. Ferrer, R.M. An Arbitrarily High Order Transport Method of the Characteristic Type for Unstructured Tetrahedral Grids. PhD Thesis, The Pennsylvania State University (2010).



9. Schunert, S. and Azmy, Y.Y. A Two-Dimensional MMS Benchmark Suite for Cartesian SN Transport Methods with Escalating Order of Nonsmoothness of the Exact Solution. *ANS Winter Meeting 2010*, Las Vegas, November 7-11 (2010).
10. Wang, Yaqi and Ragusa Jean C. On the Convergence of DGFEM Applied to the Discrete Ordinates Transport Equation for Structured and Unstructured Triangular Meshes. *Nucl. Sci. Eng.*, **163**, pp. 56-72 (2009).
11. Hesthaven, J.S. and Warburton, T. *Nodal Discontinuous Galerkin Methods*. Springer, New York & USA (2008).
12. J. M. Ruggieri, J. Tommasi, J. F. Lebrat, C. Suteau, D. Plisson-Rieunier, and C. De Saint Jean. ERANOS-2.1: The International Code System for GEN-IV Fast Reactor analysis. In *Proceedings of International Congress on Advances in Nuclear Power Plants, USA, June 4-8, 2006*.
13. Zamonsky, O.M. and Buscaglia, G.C. and Azmy, Y.Y. Improving The Accuracy of High-Order Nodal Transport Methods. *Mathematics and Computation, Reactor Physics and Environmental Analysis in Nuclear Applications*, Madrid, Spain (1999).